Altered brain-ventricle coupling modes over Alzheimer's disease progression detected with fMRI

Campo, Fulvia Francesca [1,2]; Brattico, Elvira [1,2]; Magalhães, Vicente [3]; Nigro, Salvatore [4,5]; Tafuri, Benedetta [5]; the Alzheimer's Disease Neuroimaging Initiative [+]; Logroscino, Giancarlo [5,6]; Cabral, Joana [7*]

[1] Department of Education, Psychology, Communication, University of Bari Aldo Moro, Bari, Italy

[2] Center for Music in the Brain, Department of Clinical Medicine, Aarhus University & The Royal Academy of Music Aarhus/Aalborg, Aarhus, Denmark

[3] Department of Cognitive Science, Faculty of Medicine, Faculty of Psychology, Faculty of Sciences, School of Arts and Humanities, University of Lisbon, Portugal

[4] Institute of Nanotechnology, National Research Council (CNR-NANOTEC), c/o Campus Ecotekne, via Monteroni, 73100 Lecce, Italy

[5] Center for Neurodegenerative Diseases and the Aging Brain, Department of Clinical Research in Neurology, University of Bari "Aldo Moro", "Pia Fondazione Cardinale G. Panico", Tricase, Lecce, Italy

[6] Department of Basic Medicine, Neuroscience, and Sense Organs, University of Bari "Aldo Moro", Bari, Italy

[7] Life and Health Sciences Research Institute (ICVS), School of Medicine, University of Minho, Braga, Portugal

[+] Data used in preparation of this article were obtained from the Alzheimer's Disease Neuroimaging Initiative (ADNI) database (adni.loni.usc.edu). As such, the investigators within the ADNI contributed to the design and implementation of ADNI and/or provided data but did not participate in analysis or writing of this report. A complete listing of ADNI investigators can be found at:

http://adni.loni.usc.edu/wp-content/uploads/how_to_apply/ADNI_Acknowledgement_List.pdf

*Corresponding author: Joana Cabral

joanacabral@med.uminho.pt

Life and Health Sciences Research Institute, School of Medicine, University of Minho, Portugal

Abstract

The origins of resting-state functional MRI (rsfMRI) signal fluctuations remain debated. Recent evidence shows coupling between global cortical rsfMRI signals and cerebrospinal fluid inflow in the fourth ventricle, increasing during sleep and decreasing with Alzheimer's disease (AD) progression, potentially reflecting brain clearance mechanisms. However, the existence of more complex brain-ventricle coupling modes and their relationship to cognitive decline remains unexplored.

Analyzing 599 minimally-preprocessed rsfMRI scans from 163 elderly participants across the AD spectrum, we identified distinct brain-ventricle coupling modes that differentiate across groups and correlate with cognitive scores. Beyond the known anti-phase coupling between global brain signals and ventricles —more frequent in cognitively normal controls— we discovered additional modes where specific brain areas temporarily align with ventricle signals. At the cortical level, these modes form canonical resting-state networks, such as the Default Mode Network, which occurs less in AD or the Frontoparietal Network, which correlates positively with memory scores.

The direct link between ventricle and brain signals challenges the common practice of removing CSF components from rsfMRI analyses and questions the origin of cortical signal fluctuations forming functional networks, which may reflect region-specific fluid inflow patterns. These findings provide new insights into the relationship between brain clearance mechanisms and network dysfunction in neurodegenerative diseases.

1. Introduction

The neurodegeneration leading to Alzheimer's disease (AD) is preceded by chemical alterations detectable with high specificity in cerebrospinal fluid and blood plasma long before the first symptoms of cognitive decline [1–3]. The accumulation of toxic proteins such as amyloid-β (Aβ) and tau [4,5] has been linked with disruptions in clearance pathways, involving the flow of the cerebrospinal fluid (CSF) into the interstitial space and out of the brain [6–9]. Studies using functional magnetic resonance imaging (fMRI) have shown that the inflow of CSF in the 4th ventricle is negatively correlated with the average fMRI signal in gray matter [10]. Although this brain-ventricle coupling is particularly strong during deep sleep, it is also detected during wakefulness with resting-state fMRI, and was recently found to be decreased with the progression of AD in fMRI data from the Alzheimer's Disease Neuroimaging Initiative (ADNI) [9,11].

The pulsations associated with glymphatic dynamics occur at ultra-slow frequencies falling in the range typically associated with resting-state brain activity, *i.e.*, below 0.1 Hz [12], although the link between glymphatic dynamics and resting state activity - thought to indirectly reflect neuronal activity - remains underexplored. While recent studies in rodents provide evidence that optogenetically-induced neuronal activity drives self-propagating waves of cerebrospinal fluid across the brain parenchyma [13], it is unclear how these waves organize at the macroscale across the brain and their relation with long range correlations - or functional connectivity - detected with fMRI [14–16]. Even if correlated Blood-Oxygenation-Level-Dependent (BOLD) responses in distant brain regions are triggered by simultaneous increases in the metabolic demand of neurons, how neural activity organizes specific phase relationships across the brain, particularly during rest, is an ongoing subject of debate [17–19].

Most resting-state fMRI (rsfMRI) research focuses on signal fluctuations detected in cortical and subcortical gray matter alone, reporting consistent modes of functional connectivity that appear altered in distinct neurological disorders and psychiatric syndromes [20–22]. rsfMRI studies have shown that AD and mild cognitive impairment (MCI) are associated with decreased connectivity within the default mode network (DMN)—a network primarily composed of the dorsal medial prefrontal cortex (mPFC), the posterior cingulate cortex (PCC), the precuneus and the angular gyrus [23–26]. This decreased connectivity is particularly prominent between the posterior (precuneus and PCC) and anterior regions, such as the ACC and mPFC [26–29]. Other studies have also suggested the involvement of subcortical structures in the DMN, such as the amygdala, anterior and mediodorsal thalamus, basal forebrain, nucleus accumbens, medial septal nucleus, ventral tegmental area, dorsal raphe

nucleus, dopaminergic nuclei, caudate nucleus, hypothalamus, and cerebellum [30]. Some of these subcortical structures, including the basal forebrain, brainstem, amygdala, and thalamus, are not directly part of the DMN but have been found to actively modulate its activity and interplay with other networks [31–33]. Many of these regions are impaired in AD and show reduced functional connectivity (FC) with the DMN, such as the hippocampus [34–36], amygdala, thalamus, and cerebellar areas, which show reduced FC with DMN regions [37–39]. A meta-analysis by Seoane et al. [30] revealed, in particular, a cluster covering the mediodorsal nucleus, and a medial and posterior thalamic cluster covering the pulvinar complex. However, the contribution of subcortical regions to the DMN is not yet fully understood [30], as some studies highlight the importance of Crus I/II and lobule IX [40–42], while others focus on vermis X, lobule VIIIB, or the dentate gyrus nucleus [40,42,43], and still others on the basal forebrain, caudate nucleus, nucleus accumbens, and ventral tegmental area [44,45]. Although these studies focused on fMRI signals from gray matter areas alone, all these subcortical anatomical structures are closely located around brain ventricles where it is difficult to dissociate the BOLD signal from additional non-neuronal physiological components.

Alterations in resting-state fMRI are not limited to the DMN alone. AD patients also exhibit abnormal connectivity in the Salience Network (SAL) [27,46], which is thought to play a central role in switching between the DMN and the Central Executive Network (CEN) [47]. Although physiological structural and functional impairments of the SAL are commonly observed in aging [48], the AD brain shows even further reduced gray matter volume in several SAL regions, such as the dorsal ACC and mPFC, bilateral frontoinsular cortices, and the dorsolateral prefrontal cortex. This reduction is thought to contribute to a failure in efficiently switching between the DMN and the CEN, which is also impaired in AD [49–51]. Only recently, the relation with CSF signals in the ventricles was explored. Han and colleagues [11] reported that the anti-correlation between the average cortical fMR signal and the 4th ventricle (termed “global BOLD-CSF coupling”) diminished significantly with AD progression, and related with β-amyloid accumulation in the DMN [9]. This result aligns with previous findings showing that global synchronization of gray matter fMRI signals was associated with better cognitive performance in healthy elders, although the relation with ventricle signals was not explored [52].

In this study, we analyze the brain activity from ADNI2 [53] repository containing 599 rsfMRI recordings from clinically-evaluated elderly individuals, categorized across the AD spectrum as early Mild Cognitive Impairment (EMCI), late Mild Cognitive Impairment (LMCI), and AD, together with healthy cognitively normal (CN) controls. These participants were also

evaluated in relation to risk factors that are believed to impact the progression of the disease [54]: years of education, social isolation (assessed taking into account marital status and retirement status), hearing impairment, age, sex as well as cognitive functioning (for the domains of memory, executive functions, visuospatial abilities and language). Avoiding any assumption regarding the origin of the fluctuations in fMRI signals, the raw data was only minimally preprocessed, without removing physiological components. Given that the focus of this paper was to explore coupling modes in fMRI signal fluctuations, irrespective of the mechanisms driving such fluctuations - which can not be adequately determined in this dataset - , we avoid using the term BOLD-CSF coupling, as currently done in the field, opting to use the term 'brain-ventricle' coupling, given that the only differentiating factor between the fMRI signals is their anatomical location.

Taken overall, exploring the relationship between the dynamics captured with fMRI in brain ventricles and resting-state activity captured in gray matter, also with fMRI, may reveal new insights into the origin of ultra-slow oscillatory modes detected in the resting state, pointing to a role in preventing neurodegeneration and supporting healthy cognitive function.

2. Results

2.1. Occupancy of phase coupling modes changes with AD progression

Our analysis - oblivious of fMRI signal origin or anatomical location - revealed a set of phase coupling modes in fMRI signals that occurred recurrently over time and across scans, irrespective of the participants' condition. We explored the repertoire of modes obtained when clustering the data into a varying number of clusters K and report in **Figure 1** the modes obtained for K=4 clusters, which is representative of the results obtained across the entire range of K explored (the impact of varying from K will be described below).

Visualizing the phase coupling modes obtained for K=4 in sagittal, axial and coronal slices (**Figure 1 a-d**) reveals distinct patterns of fMRI signal phase relationships across the entire brain, involving brain structures extending beyond gray matter, and with clear anti-phase relationship to the ventricles. The modes are characterized by the way the phase of the fMRI signals is organized, such that all the voxels colored in green covary together in phase (*i.e.*, with a phase shift <90° with respect to the mean phase orientation, while the voxels colored in magenta vary in anti-phase (*i.e.,* with a phase shift >90°) with respect to the mean of voxels colored in green.

The *occupancy* of each mode - *i.e.*, the proportion of time instants in which a mode is detected during a scan - was calculated for each scan, and compared across conditions. The 4 coupling modes detected with K=4 varied significantly in occupancy across the progression of AD and a summary of the statistical analysis is reported in **Figure 1 a'-d'**.

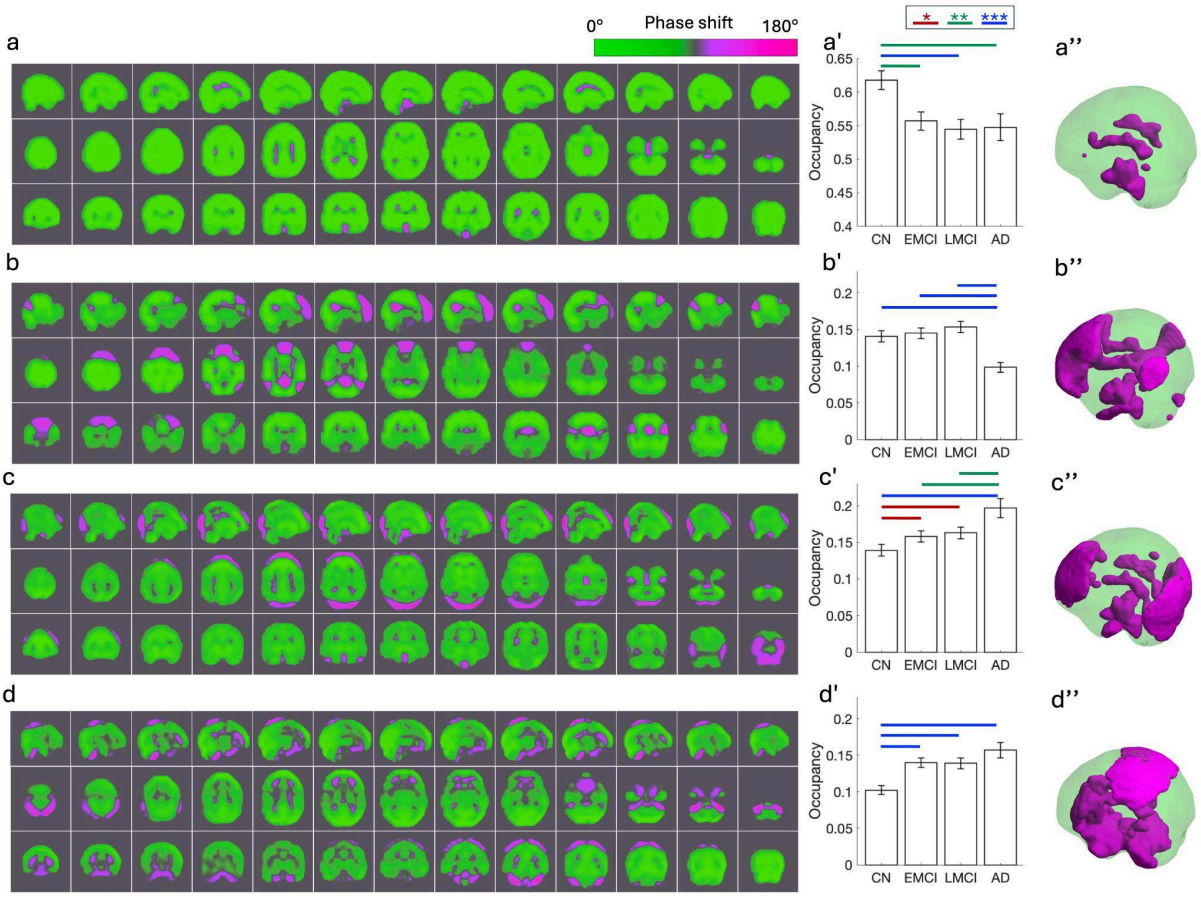

Figure 1. Phase coupling modes detected in all fMRI scans with K=4 and corresponding occupancy across conditions. Phase coupling patterns were computed between v=1821 1cm^3 brain voxels (covering both gray matter, white matter and ventricles) for each instant of time for all the s=599 scans, irrespective of the participant's condition. The resulting 81707 phase coupling patterns (obtained as the leading eigenvectors of the cosine of phase differences at each time point) were clustered into K=4 clusters. (**a-d)** Each of the 4 cluster centroids corresponds to a recurrent mode of phase coupling detected in the data, where voxels colored with the same color vary in phase, and voxels in different colors vary in anti-phase. Each coupling mode is shown in sagittal (top), axial (middle), and coronal (bottom) equidistant slices. (**a'-d'**) The proportion of time points during which a mode is detected, or *Occupancy*, was calculated for each scan and compared across conditions. Error bars report the mean $\pm$ the standard error of the mean (SEM) across scans in each condition. Statistical significance was determined using unpaired t-tests with 10000 permutations. Considering multiple testing, red indicates $p_{perm}<0.05$, which can be a false positive; green corresponds to $p_{perm}<0.05/4$ to consider the K=4 modes compared, and blue corresponds to $p_{perm}<0.00015$ correcting

by all comparisons across the full repertoire of modes obtained with K from 2 to 20, indicating a strong chance of a true positive. (**a''-d''**) The phase coupling modes are rendered in 3D, showing in magenta the smaller subset of regions shifting by more than 90° from the rest of the brain (green)

The first phase coupling mode (**Figure 1a**) was detected around 61.7% of the time in fMRI scans in CN (± 1.4%, mean ± standard error of the mean, SEM), and occurred significantly less in all other 3 conditions, namely EMCI (55.6% ±1.3, p_{perm}=0.0010), LMCI (54.4% ±1.4, p_{perm}=0.00012), and AD (54.7% ± 2.01, p_{perm}=0.0020). Both EMCI, LMCI and AD exhibited similar occupancy of this mode, p_{perm}>0.25). This mode corresponds to an activity pattern where the fMRI signals in voxels colored in magenta - revealing the 2 lateral ventricles and the 3rd and 4rth ventricles - vary with a phase shift larger than 90° with respect to the rest of the brain.

The second coupling mode (**Figure 1b**) was found to decrease its occupancy only in AD, being detected 9.85 ± 0.67 of the time in fMRI scans from AD patients, while it occurred 14.1% ± 0.7 in CN, 14.5% ± 0.7 in EMCI, and 15.3% ± 0.8 in LMCI (p_{perm}=0.000069 CN vs AD; p_{perm}=0.00001 EMCI vs AD; p_{perm}=0.00000011 LMCI vs AD). In this mode, the voxels shifting in phase with respect to the rest of the brain (colored in magenta) extend beyond the ventricles, revealing large brain areas where the signals shift out of phase from the global fMRI signal (these brain areas are characterized in more detail in the following sections).

The two other phase coupling modes obtained with K=4 were found to increase their occurrence over the progression of AD. Mode 3 (**Figure 1c**), detected around 13.9% ± 0.8 of the time in CN, was found to increase to 15.8% ± 0.8 in EMCI (p_{perm}=0.046 CN vs EMCI), to 16.3% ± 0.8 in LMCI (p_{perm}= 0.02 CN vs LMCI) and to 19.7% ± 1.2 in AD patients (p_{perm}=0.000039 CN vs AD, p_{perm}=0.0045 EMCI to AD and p_{perm}=0.012 LMCI to AD). Similarly to the other coupling modes, no differences were detected between EMCI and LMCI (p_{perm}>0.05).

The 4th coupling mode (**Figure 1d**) occurs around 15.7% ± 1.05 of the time in AD while only 10.2% ± 0.59 in CN, differing with p_{perm}=0.000000013, the most significant difference detected in this study. Notably, this mode already differs between CN and EMCI (14.0% ± 0.63, p_{perm}=0.0000093) and LMCI with a similar occurrence of and 13.9% ± 0.73, significantly differing from CN with and p_{perm}=0.00012 respectively, indicating that it becomes altered in the first stages of the disease. Similarly to mode 2, the patterns of phase coupling observed in modes 3 and 4 reveal distinct brain areas whose signals shift out of phase from the global brain signal (green) and align with the activity inside the ventricles (magenta).

2.2. Consistent phase shifted signals between brain and ventricles

We extended our analysis to the entire repertoire of phase coupling modes obtained when varying the number of clusters K between K=2 to K=20, given that the process of determining the optimal number of clusters in k-means clustering is inherently subjective, and different evaluation metrics like silhouette scores and Dunn's index may suggest optimal values that might not capture the most meaningful grouping for distinguishing across conditions. Despite the apparent complexity of patterns detected, they all share one particular property: the ventricles are consistently found within the group of voxels whose signals evolve in opposite direction from the majority of voxels in the brain (rendered in magenta in **Figure 2).** Moreover, for all partitions into K clusters, the most frequently detected cluster (c=1, first column in **Figure 2**) corresponds to the same mode of phase coupling where the fMRI signals in the ventricles are shifted out of phase from the rest of the brain. In agreement with previous studies, this 'global brain vs. ventricles' mode (Mode 1) was found to decrease in AD, but this change becomes less significant as the number of clusters increases and more complex brain-ventricle coupling modes are included in the partition.

Across the entire repertoire of 209 clusters obtained with K from 2 to 20,a substantial portion of these (~25%) was found to differ significantly in occupancy between CN and AD (surviving conservative corrections for multiple comparisons and with medium-to-large effect sizes, see **Supplementary Figure S1**). Given that some of the clusters detected across K share strong spatial similarities, we compared the cluster centroids differentiating between CN and AD and grouped them into 5 modes of phase coupling according to their spatial similarity (Pearson's r>0.85, **Supplementary Figure S9**). The first 4 modes, highlighted with different color shades in **Figure 2**, correspond to the modes detected with K=4 reported in **Figure 1.** Apart from these 4 modes of phase coupling, a 5th mode, detected for K≥17 (highlighted with a black box), was found to decrease significantly in AD (this mode will be explored in more detail in section 2.4. *Brain-Ventricle coupling modes reveal Resting-state Networks*).

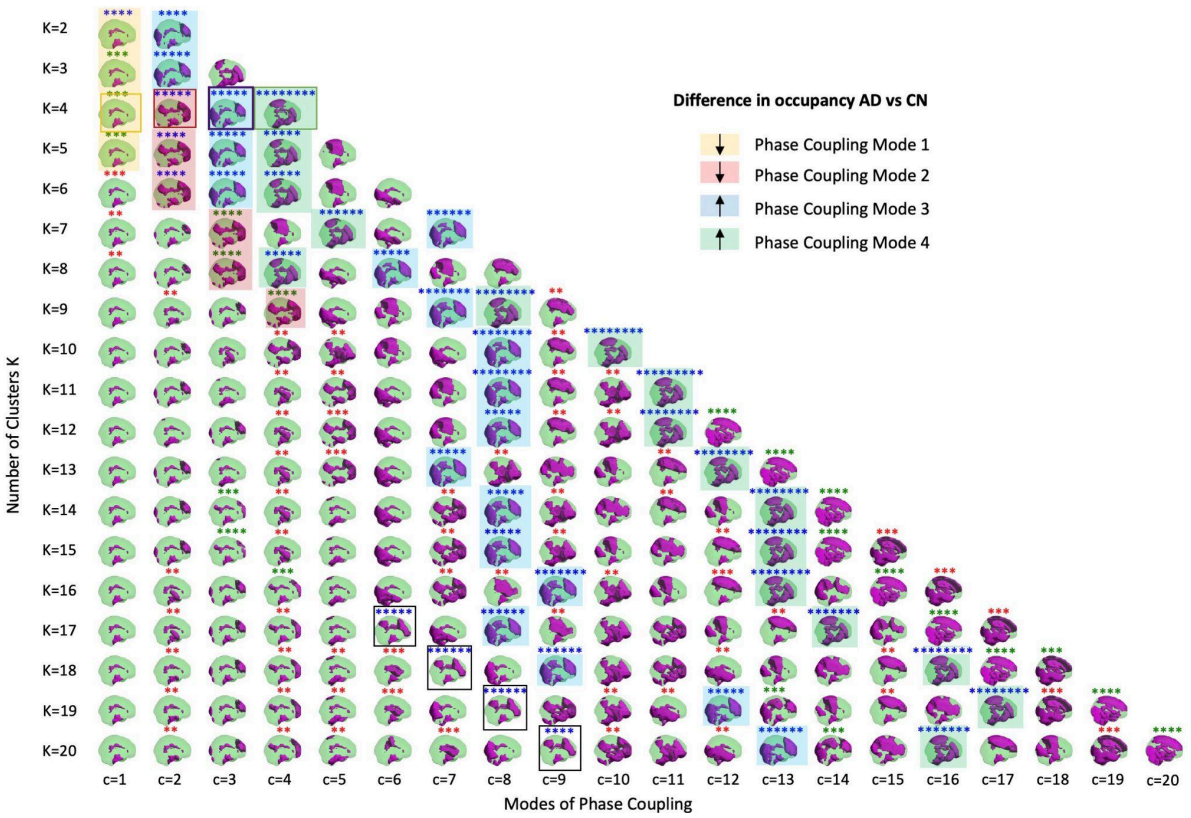

Figure 2 - Consistent Modes of Phase Coupling occurring differently in AD. Pyramid showing all the phase coupling modes detected when varying the number of clusters (K) from 2 to 20, sorted from left to right according to their average occupancy0, and highlighting the ones that occurred differently in AD vs CN. Each mode is represented by the corresponding cluster centroid (c) shown in a transparent brain viewed from the side, rendering in magenta all voxels whose fMRI signals are phase-shifted by more than 90° relative to the rest of the brain. The number of asterisks on top of the modes represent the number of decimal cases in p-values from permutation tests between occurrence in AD vs CN, with colors indicating the level of statistical significance: red for $p_{perm} < 0.05$; green for $p_{perm} < 0.05/K$ accounting for K independent comparisons; and blue for $p_{perm} < 0.05/\sum(k=2:k=25) = 0.00015$, correcting for both independent and dependent comparisons across the full set of modes compared. Overall, our statistical analysis revealed two modes occurring less in AD compared to CN (modes 1 and 2, indicated by yellow and red shades), and two other modes with higher occupancy in AD compared to CN (modes 3 and 4, indicated by blue and green shades). The empty black boxes indicate an additional mode of phase coupling decreased in AD detected for K≥ 17.

Although the most significant differences in this study were detected between the CN and AD groups, our results also revealed significant differences across the different stages of cognitive decline (CN, EMCI, LMCI, AD). In the transition from CN to EMCI, the most significant difference is an increase in the occupancy of the Phase Coupling Mode 4, (with p_{perm} = 0.000009 for K=4, C=4) and a decrease in the occupancy of the Phase Coupling Mode 1, (p_{perm} = 0.00019 for K=20, C=2). As shown in **Supplementary Figures S1 to S8**,

the pair of conditions showing less between-group differences in mode occurrence were EMCI and with LMCI, and statistical differences were detected only when increasing the number of clusters to K=12, C=2 (*cfr*. **Supplementary Figure S6**), where one specific coupling mode decreases significantly from EMCI to LMCI, with p_{perm}=0.0035. However, this difference only survives Bonferroni correction at that specific clustering partition, becoming less significant for larger numbers of clusters (*e.g.*, K =18, C=2; K=19, C=2; K=20, C=2). Between LMCI to AD, the main difference is a decrease in Phase Coupling Mode 2 (most significant for K=4, C=2, with p_{perm}= 0.0000001), and a decrease in Mode 5 detected for finer grained partitions (most significant for K=17, C=6, p_{perm}= 0.0000015). This reveals that different conditions may reflect changes in different patterns, which are optimally detected at different levels of granularity, justifying the extended analysis across a broad range of K.

2.3 Brain activity as a temporal sequence of phase coupling modes

Each fMRI volume recorded at each instant of time (with Time of Repetition, TR=3 seconds) is assigned to one mode, such that brain activity over an entire scan can be represented as a temporal sequence of modes. **Figure 3a** shows the fMRI signals over time, with colored shades indicating the cluster assignment at each instant of time obtained with K=4 for a scan from a control participant. As can be seen, modes 1 and 2 are more frequently detected than modes 3 and 4 during this scan.

As illustrated in **Figure 3b**, an occurrence of mode 2 corresponds to the periods of time when the fMRI signals in specific voxels either co-increase above the mean (*e.g*. at t = 4, 41, 77, 104 and 117) or co-decrease below the mean (t = 19, 50, 87, 100), while the fMRI signals in the other voxels vary in the opposite direction. Although the instantaneous snapshots of fMRI signals are very noisy, the pattern associated with Mode 2 is clearly visible, particularly around axial slice sl=54. In **Figure 3c**, we show the fMRI signals during two occurrences of Mode 1, one at t = 35 when the brain signals are globally above the mean (red) and another at t = 73 when the brain signals are globally below the mean (blue). Although the ventricles are not clearly visible, a close inspection to slices sl=26 to sl=50 shows fMRI signals with opposite sign in voxels overlapping with ventricle locations in the standard MNI brain template shown in **Figure 3d**.

Given that the k-means clustering employs a winner-take-all approach, each time point is assigned to a single cluster. However, this does not exclude the possibility that multiple coupling modes co-occur in the brain simultaneously, explaining the complexity of patterns

observed at the instantaneous level (*e.g.* in **Figure 3b**, at time t=50, Mode 2 is visible in slice 50 while a different mode of coupling is visible in slice 30).

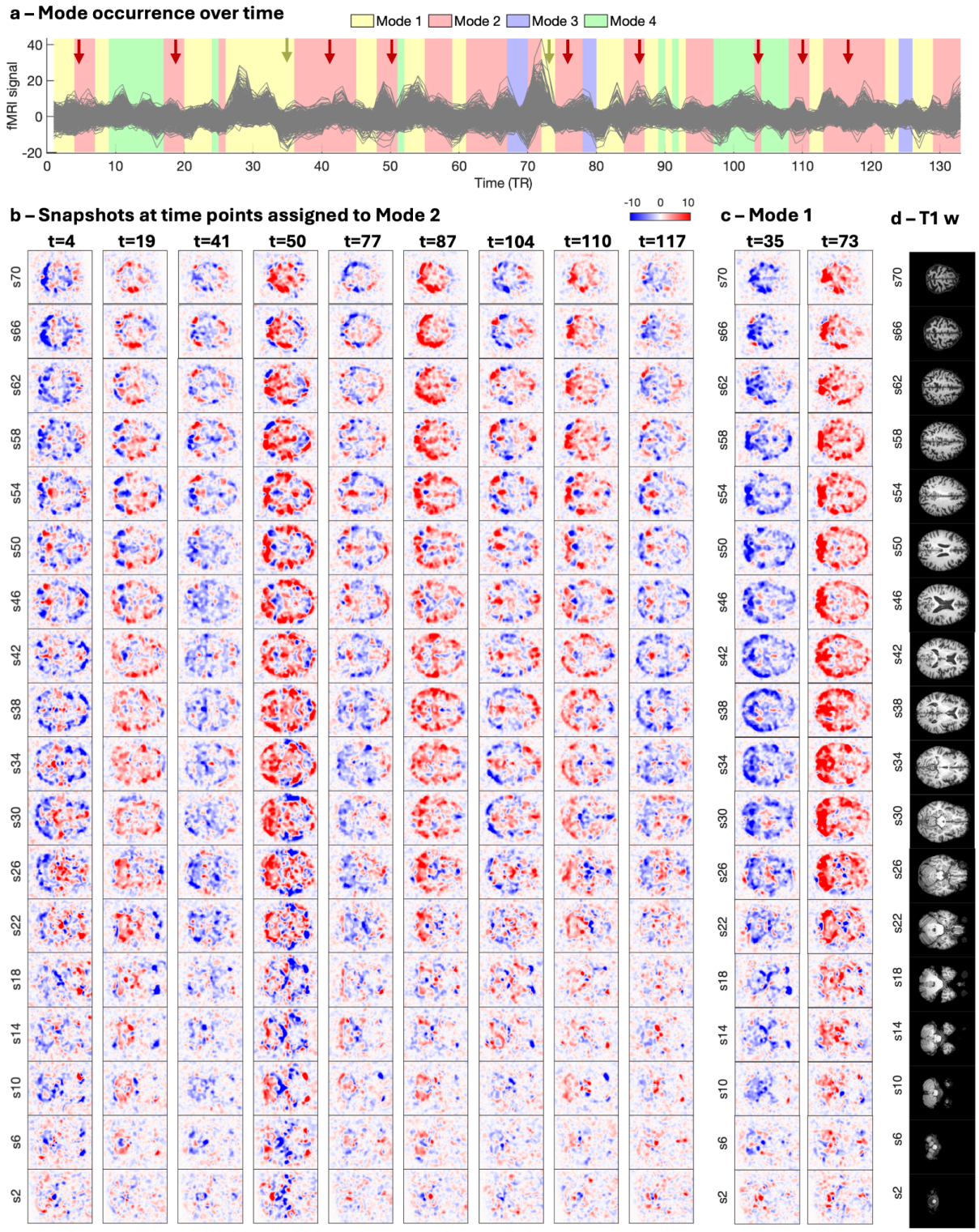

Figure 3 - Occurrence of phase coupling modes over time. a. The fMRI signals recorded in 135 instants of time, with a TR of 3 seconds, are plotted for the entire scan duration from a CN participant (preprocessed signals with mean removed). The colored shades indicate the mode of phase coupling dominating in each instant of time. **b.** Snapshots of fMRI volumes (showing equidistant axial slices

from top to bottom) obtained in time points assigned to Mode 2 (corresponding to the red arrow locations in panel a). **c.** Snapshots of time points assigned to Mode 1. **d**. T1-weighted MPRAGE from the same subject normalized to MNI space showing the same axial slices shown in panels b. and c.

2.4. Brain-Ventricle coupling modes reveal Resting-state Networks

The brain areas shifting in phase by more than 90° relative to the rest of the brain form a functional network with temporally correlated activity. To investigate how the modes of phase coupling relate with canonical resting-state networks, we computed the overlap between the set of voxels shifting in phase located in the cortex alone and the seven resting-state networks from a widely used template [55], defined on the same cortical voxels. In **Figure 4**, we color the modes of phase coupling exhibiting a strong overlap (Pearson's correlation >0.35) with the 7 resting state networks used as reference.

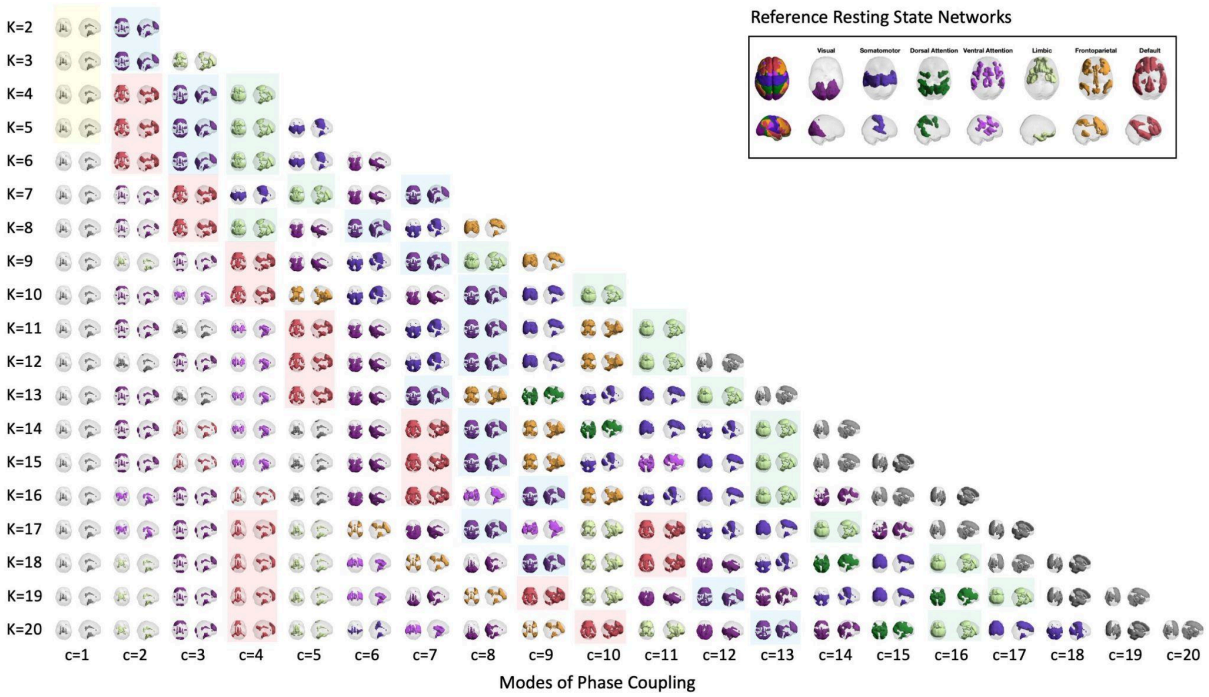

Figure 4. Modes of phase coupling overlap with resting state networks. Pyramid showing all the phase coupling modes detected with K from 2 to 20, highlighting in different colors all voxels whose fMRI signals are phase-shifted by more than 90° relative to the rest of the brain. The colors correspond to the resting-state networks from the template defined in [55]: red for the Default Mode Network (DMN), purple for the visual network, blue for the somatomotor network, green for the dorsal attention network, light purple for the ventral attention network, light green for the limbic network, and yellow for the frontoparietal network (FPN). Networks in gray do not correlate with any of the reference networks. The colored shades (yellow for mode 1, red for mode 2, purple for mode 3, and green for mode 4) illustrate the variations of these modes as the number of clusters increases.

Our analysis reveals that several of the phase coupling modes detected, when considering the cortical voxels alone, share spatial similarities with known resting-state networks. For instance, Mode 2 is found to overlap strongly with the DMN (red, r=0.60, shown in detail in **Figure 5** top left). This mode overlapping with the DMN is consistently detected for K ranging from 4 to 20. Notably, starting from K=17, the clustering divides the DMN into two different clusters (K17, C4 and C11; K18, C4 and C11; K19, C4 and C9; K20, C4 and C10) and a new cluster appears, showing strong overlap with the lateral Fronto-Parietal Network (red, r=0.60, **Figure 5** bottom right).

Other modes were found to overlap with the different RSNs used as reference. Although Mode 3 exhibits some overlap with the visual network, given that some voxels are in the Occipital cortex, the correlation is lower because some voxels are in the frontal cortex (r=0.45, **Figure 5** top middle). As K increases to K=6, we detect a mode overlapping more closely with the visual network (r=0.67, **Figure 5** bottom middle), although this mode did not differ in occupancy between any of the 4 conditions. Another mode detected with K=6 and not showing any significant difference between conditions overlaps with the Somatomotor network (r=0.57, **Figure 5** bottom left).

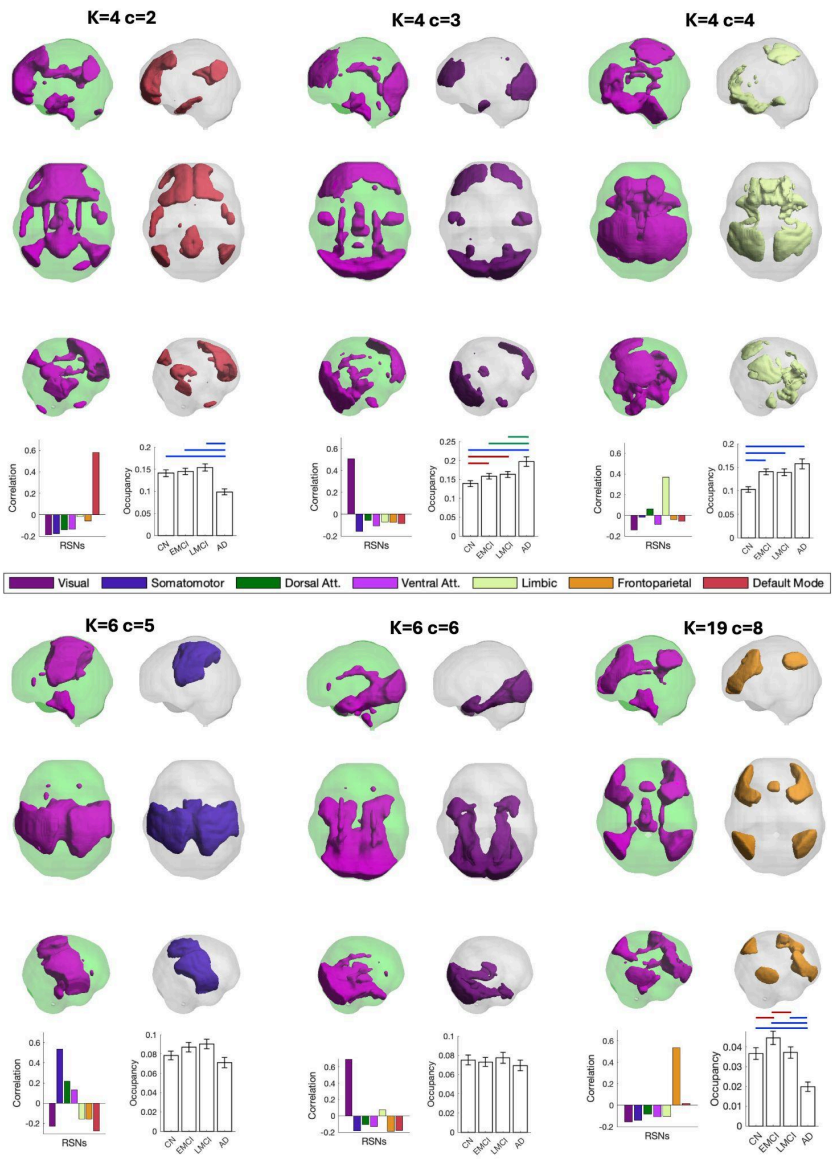

Figure 5. Regions of resting state networks align in phase with fMRI signals in the ventricles. The phase coupling modes detected in the entire brain (considering all voxels within an MNI brain mask, irrespective of their anatomical location) reveal modes of phase coupling between cortical voxels and ventricular voxels. The colored overlays on brain models indicate specific RSNs: visual (purple), somatomotor (blue), dorsal attention (green), ventral attention (light purple), limbic (light green), frontoparietal (orange), and default mode (red). The correlation bar plots show the spatial overlap of each mode with classical RSNs, while the occupancy bar plots represent the frequency of each mode across conditions. Statistical significance was assessed using unpaired t-tests with 10,000 permutation tests, considering multiple comparisons. Red lines indicate $p_{perm} < 0.05$, which may represent false positives due to multiple testing. Green corresponds to $p_{perm} < 0.05/20$, and blue corresponds to $p_{perm} < 0.00015$, adjusting for all comparisons across the full range of modes with K values from 2 to 20, indicating a high likelihood of a true positive.

Overlapping the cluster centroids with the AAL2 parcellation into 120 anatomical cortical and subcortical gray matter areas, reveals that the voxels aligning in phase with the ventricle signals in Mode 2 correspond to brain areas known to belong to the DMN, with most voxels in the Medial Frontal Superior cortex, the Medial Orbitofrontal cortex, the Angular gyrus, the Anterior and Posterior Cingulate cortex, and even some voxels in Inferior and Middle Temporal Cortex (all including left and right parcels). A complete list of AAL2 brain areas for each mode can be found on **Supplementary Figure S10.**

In Mode 3, most voxels are located in the occipital cortex (including the inferior, middle, and superior regions), the cerebellum, and the frontal cortex (including the superior, middle, and inferior regions). Additional voxels are found in the middle and inferior temporal gyri and the lateral occipitotemporal gyrus, covering the lingual and fusiform gyri and the calcarine fissure.

In Mode 4, most voxels aligning in phase with the ventricles are distributed in temporal regions (such as the superior and middle temporal pole, middle and inferior temporal gyrus, and fusiform gyrus) and parietal areas (including the superior parietal gyrus, inferior parietal lobule, angular gyrus, and precuneus). The cerebellum also contains a significant number of voxels, spanning several lobules, as well as Cerebellar Crus, and segments of the cerebellar Vermis. Additional voxels are present in frontal regions, including the superior, middle, and inferior frontal gyri, the anterior, medial, and posterior orbital cortex, and the gyrus rectus.

2.5. Comparisons with scores

We examined how the occupancy of the 4 functional coupling modes detected with K=4 correlated with the different ADNI cognitive composite cognitive scores as well as age and years of scholar education. The Pearson's correlation coefficients (r) and their associated p-values are reported in **Table 1**.

	Mode 1 Occupancy		Mode 2 Occupancy		Mode 3 Occupancy		Mode 4 Occupancy	
	r	p-value	r	p-value	r	p-value	r	p-value
Memory	0.097	* 0.040	**0.16**	*** **0.00051**	**-0.16**	*** **0.00089**	**-0.18**	*** **0.00015**
Executive Function	0.096	* 0.044	**0.13**	** **0.0072**	**-0.13**	** **0.0076**	**-0.17**	*** **0.00036**
Language	0.060	0.20	**0.13**	** **0.0039**	-0.10	* 0.028	**-0.14**	** **0.0032**
Visuo-Spatial	0.048	0.43	**0.21**	*** **0.00043**	-0.13	* 0.026	-0.14	* 0.019

Age	0.10	* 0.013	**-0.14**	*** **0.00055**	0.0077	0.85	-0.071	0.081
Education	0.074	0.071	-0.0025	0.95	-0.089	* 0.030	-0.043	0.30

Table 1. Correlations between phase-coupling mode occupancy and 10 scores. Each variable's correlation with each mode is presented as a Pearson correlation coefficient r alongside its associated p-value. Asterisks indicate the level of statistical significance, with * for p<0.05, ** for p<0.05/4, *** for p<0.05/4/6 (Bonferroni-corrected).

While the occupancy of Mode 1 did not show any relations surviving corrections for multiple comparisons, the occupancy of coupling Mode 2, which significantly overlaps with the DMN at the cortical level, was found to correlate positively with all four cognitive scores for Memory, Executive Function, Language and Visuospatial abilities, while negatively correlating with Age. Conversely, Modes 3 and 4 did not show any relation with Age, but correlated negatively with Memory and Executive function. Mode 4 also correlated negatively with Language scores.

Other binary metrics were compared, such as Marital Status, Retirement Status, Hearing Impairment and Sex (**table 2**). We found a strong relationship between all Mode Occupancy and Sex (p_{perm}=0.00000016, p_{perm}=0.00000014, p_{perm}=0.0095 and p_{perm}=0.00000013 respectively for Mode 1, 2, 3 and 4), and a significant relationship between Mode 1 and Marital Status (p_{perm}=0.0086).

		Mode 1		**Mode 2**		**Mode 3**		**Mode 4**	
		r (± STD)	p-value	r (± STD)	p-value	r (± STD)	p-value	r (± STD)	p-value
Marital Status	M	0.578 (± 0.09)	***0.0086**	0.135 (± 0.004)	0.031	0.156 (± 0.005)	0.076	0.131 (± 0.004)	0.15
	NM	0.535 (± 0.015)		0.148 (± 0.008)		0.176 (± 0.010)		0.140 (± 0.008)	
Retirement Status	W	0.561 (± 0.019)	0.34	0.148 (± 0.011)	0.49	0.161 (± 0.011)	0.14	0.130 (± 0.009)	0.38
	NW	0.569 (± 0.008)		0.136 (± 0.004)		0.161 (± 0.005)		0.134 (± 0.004)	
Hearing Impairment	NH	0.564 (± 0.008)	0.078	0.139 (± 0.004)	0.22	0.163 (± 0.005)	0.16	0.134 (± 0.004)	0.18
	HI	0.595 (± 0.019)		0.128 (± 0.010)		0.153 (± 0.011)		0.124 (± 0.008)	
Sex	M	0.618 (± 0.010)	****0.000 00016**	0.129 (± 0.005)	****0.0000 0014**	0.137 (± 0.006)	***0.0095**	0.116 (± 0.005)	****0.000 00013**
	F	0.516 (± 0.011)		0.147 (± 0.006)		0.186 (± 0.007)		0.151 (± 0.006)	

Table 2. Mean occupancy (Pearson correlation coefficient r) and standard error of the mean (STD), and associated p-values from 10000 permutations of each binary metric: marital status (M= married, NM = unmarried), retirement status (W= working, NW = not working), hearing impairment (NH = normal hearing; HI = hearing impaired) and sex (M= male, F = Female), across the four coupling modes. Asterisks indicate the level of statistical significance, with * for $p<0.05$, and ** for $p<0.05/4/4$.

Extending the analysis beyond the selected partition into K=4 to the entire range of modes, reveals interesting relationships, surviving the most stringent correction for multiple testing, setting a significance threshold of p=0.05/209/10=0.000024, given that 10 scores were compared for 209 modes (cyan line in **Figure 6**). This extended yet stringent analysis revealed that the Memory Composite score correlates positively (r=0.21, p= 0.0000089) with the occurrence of the coupling mode obtained for K=19, c=8 which overlaps, at the cortical level, with the latero-Frontoparietal network, usually referred to in the literature as the Executive Control Network. Another cluster obtained for K=11, c=11, which corresponds to Coupling Mode 4, is the one that most strongly correlates (negatively) with the Executive Function (r=-0.199, p=0.000024) composite score.

Our results also reveal that the set of asymmetric coupling modes detected rarely, yet consistently for $K\geq12$, occur more often in participants with low Visuospatial abilities (r=-0.299, p=0.00000047 for K=13, c=13), also correlating negatively - although less significantly - with Language, Executive Function, Memory and years of scholar education. Although no cluster was found to correlate significantly with the Language composite score.

Finally, a mode of coupling where the left and right Insula align in phase with the signals in the ventricles was found to correlate positively with age, detected consistently for K=10, 13-20, being most significant for K=17, c=2 (r=0.226, p-value=0.0000000232).

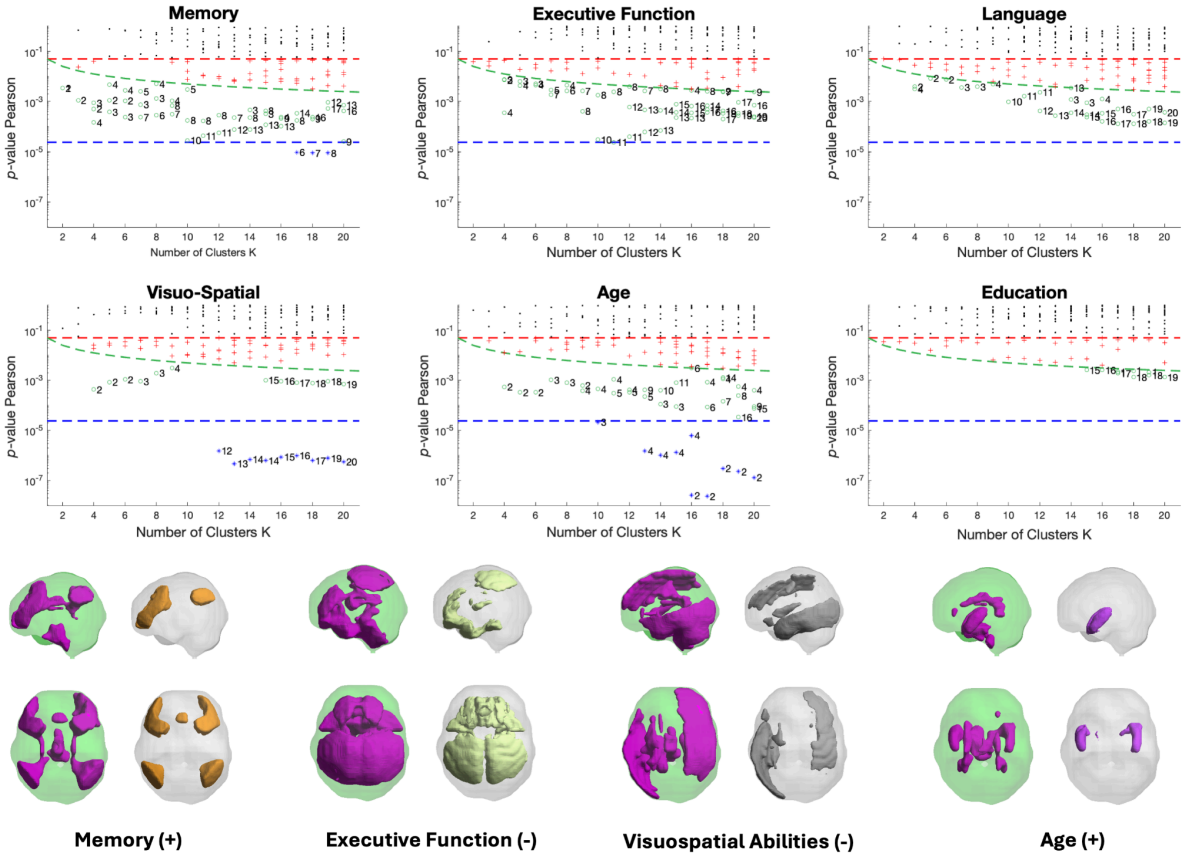

Figure 6. Statistical comparisons between mode occupancy and continuous variables. Pearson's correlation was computed between the occupancy of each mode obtained for the entire range of K explored and the four ADNI composite cognitive scores as well as age and years of scholar education. **top panel:** p-values are reported for the 6 different variables considered where colors indicate the level of statistical significance, with red representing $p_{perm} < 0.05$, green $p_{perm} < 0.05/K$ and blue representing the most stringent FWER correction with $p_{perm} < 0.000024$ accounting for all the comparisons made with the 10 continuous and binary scores. **bottom panel:** the cluster centroids (or modes) obtained for K=19, C=8; K=11, C11; K=13, C=13; K=17, C=2, showing for each mode (left) a magenta patch representing all the voxels shifting by more than 90° with respect to the main orientation of fMRI signals and (right) a patch containing only the cortical voxels and colored according to the RSN to which they overlap the most.

3. Discussion

This study provides novel insights into brain coupling dynamics by analyzing fMRI signals without distinguishing between ventricular and cortical sources. Our approach reveals new perspectives on neural connectivity and offers a unique lens through which to examine brain function. For the first time, we present an analysis that bridges the gap between resting state dynamics and glymphatic pulsations, converging two distinct fields in neuroimaging

research. While we observed highly significant alterations across AD progression, it is important to note that our findings are based on an existing open-source database with inherent limitations. As such, the precise origin of the signals, the mechanisms organizing them across space, and their specific role in brain function remain to be fully elucidated. Nevertheless, this work lays the ground for a more comprehensive understanding of brain dynamics that encompasses both neural and non-neural components of brain physiology.

Our innovative analysis approach identified four main modes of brain-ventricle coupling that change significantly with AD progression. Two of these phase coupling modes decreased from CN to AD (modes 1 and 2), while two others (modes 3 and 4) increased from CN to AD.

Notably, Phase coupling mode 1 exhibits phase synchronization across nearly the entire brain, consistently with Han et al. [11], who explored the coupling between the global brain signal and CSF fluid. In their study, the authors used a subset of the ADNI 2 dataset, focusing on subjects who had both rsfMRI and PET measurements, as well as Mini-Mental State Examination (MMSE) scores. Our study replicates their findings with a larger sample size (due to less stringent inclusion criteria) and, consequently, greater statistical power.

While the first coupling mode has already been subject of studies, the other three coupling modes have a more complex configuration. To our knowledge, the relationship between brain-ventricle coupling at rest and RSNs has not yet been fully clarified. Despite the accumulating evidence demonstrating their relation with healthy and pathological brain function, the physiological nature of 'intrinsic connectivity networks (ICNs)', 'resting-state networks (RSNs)' or 'functional gradients' has not been fully disambiguated [16,56]. While there have been attempts to propose that RSNs are associated with physiological components of the brain, the field of fMRI research generally assumes that the fMRI signals in the gray matter areas, once adequately preprocessed to remove physiological components, are associated with the BOLD signal, directly associated with neurovascular coupling. Here, we do not directly exclude this hypothesis, but avoid using the term BOLD to refer to fMRI signals from gray matter, because we believe further studies are needed to determine whether resting-state signal fluctuations are strictly BOLD-related or have a more direct relationship with the fMRI signals in the ventricles, potentially linked with CSF inflow/outflow into the brain. Given the limitations of the current dataset, our focus was on exploring the existence of coupling modes between distinct brain structures extending beyond gray matter alone and the conventional BOLD paradigm, to better understand the dynamical alterations in brain activity accompanying the progression of cognitive decline.

3.1 Phase coupling differences across conditions

Four modes show significant differences across the transition from CN to AD (**Figure 7**). Notably, the transition from CN to EMCI is characterized by an increase in the limbic network (corresponding to Coupling Phase Mode 3) and a decrease in Coupling Phase Mode 1, where the activity in the two lateral ventricles and the fourth ventricle exhibits a phase shift greater than 90° relative to the rest of the brain.

Previous research has already attempted to explore the transition from CN individuals to EMCI from the perspective of RSNs. For instance, McKenna et al. [57] used a subset of the ADNI dataset and incorporated the presence of the Apolipoprotein E allele e4 (APOE e4) as a covariate. Consistent with our findings, their study revealed disrupted connectivity in EMCI, particularly in key regions such as the cingulate cortex and its connections with anterior and posterior MPFC. Moreover, they observed that this functional connectivity disruption is strongly linked to levels of the APOE e4 protein in CSF samples [57]. Although there are differences in the methodologies between our study and theirs, it is plausible that the results we have obtained could be associated with this genetic factor. However, a comprehensive understanding of the role of genetics in the observed functional coupling alterations requires further investigation.

Since we detected significant alterations in functional coupling already at the EMCI stage, we cannot exclude the possibility that these changes may occur even before the biochemical alterations become evident. It remains unclear whether the biochemical alterations precede the disruptions in brain-ventricle coupling, or if the latter occur at earlier stages. Further research is needed to clarify the sequence of these events and whether the observed functional connectivity changes might serve as an early indicator of AD progression, possibly even before the biochemical markers are detectable.

The transition between LMCI and AD is characterized by a fall in the occurrence of the DMN (corresponding to the Coupling Phase Mode 4) and of the frontoparietal network (FPN).

Interestingly, the frontoparietal network, which is significantly reduced in AD, shows a progressive decrease from EMCI to LMCI and from LMCI to AD, with the significance increasing in the latter comparison. However, it appears with higher occurrence in the EMCI group compared to CN (**Supplementary figure S3**). The p-value does not survive any of our corrections for multiple comparisons, suggesting that this finding could likely be a false positive, potentially due to outliers in the EMCI group.

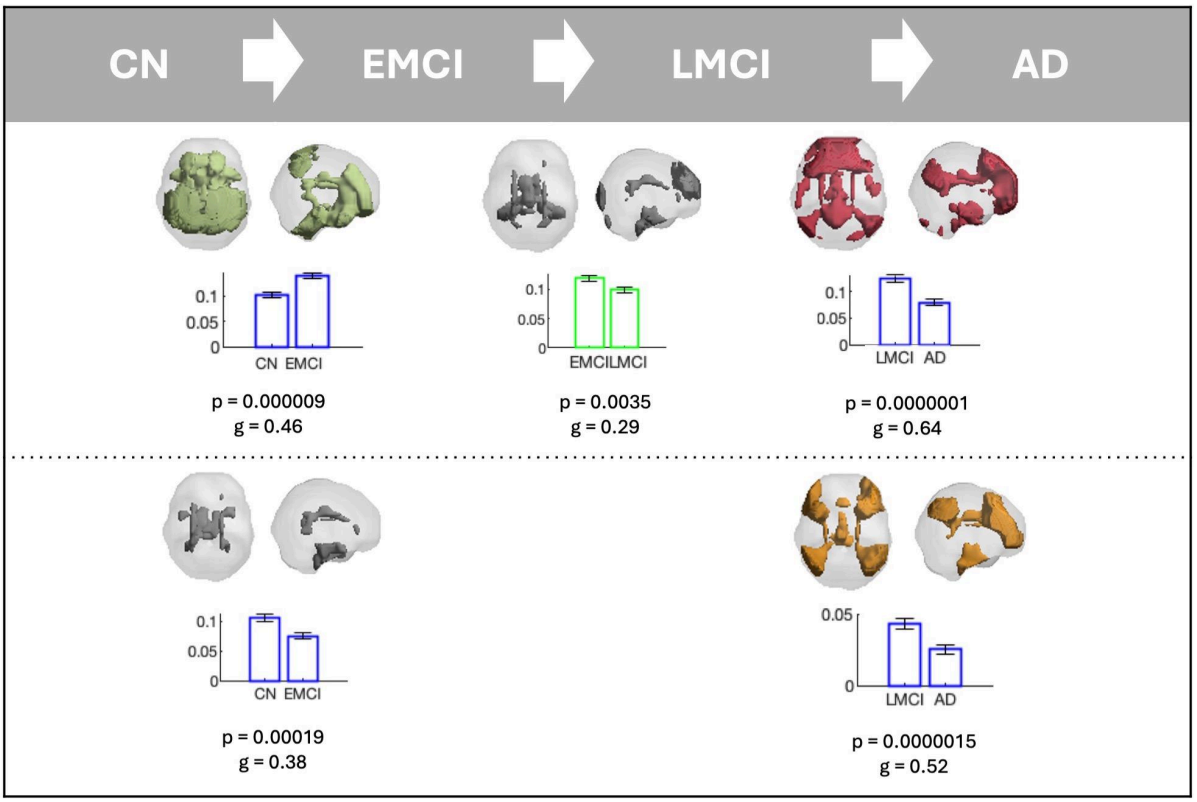

Figure 7. Functional coupling modes associated with transitions between AD progression stages. In the transition from CN to EMCI, two modes significantly differ: the phase coupling mode that overlaps with the limbic network, which corresponds to the Phase Coupling Mode 4, higher in EMCI than CN, and a network that corresponds to the Phase Coupling Mode 1, higher in CN than EMCI. In the transition between EMCI to LMCI a statistical difference was found in the Phase Coupling Mode 1. In the transition between LMCI to AD other two networks are involved: the DMN, corresponding to the Phase Coupling Mode 2, and the frontoparietal network, both higher in LMCI than AD. The color patches indicate all voxels whose fMRI signals are phase-shifted by more than 90° relative to the rest of the brain. The colors correspond to the classic "Yeo" networks [55]: red for the DMN, light green for the limbic network, and yellow for the frontoparietal network. Voxels in gray represent regions that do not overlap with any of the previously mentioned networks.

Other attempts to assess functional brain connectivity alterations in different stages of neurodegeneration have been made, though with certain limitations, such as using a small subsample of the ADNI2 database, which reduces the statistical power of the study [58]. In their study, they did not find significant differences in the DMN, except in the EMCI group. In contrast, our study identified differences in the DMN when comparing CN vs. AD, EMCI vs. AD, and LMCI vs. AD (see **Supplementary Figures S5, S7, S8**).

Interestingly, regions within DMN are among the first areas where Aβ deposition begins, occurring years before a formal AD diagnosis. In particular, it was seen that global glymphatic function—measured by the coupling between global brain activity and the CSF

flow—has a strong association with various Aβ and tau markers at the early stages of AD pathology. This suggests that resting-state global brain activity may influence Aβ accumulation in the initial stages of the pathology, likely through its effect on glymphatic clearance. The spatial differentiation of this activity further highlights how certain brain regions may be more vulnerable due to impaired glymphatic function [9].

Coupling Phase Mode 1, which decreases in AD compared to CN, reveals that the so-called "global signal" is phase-shifted by more than 90° relative to the signal from the ventricles. While the prevalence of the global signal was previously reported to relate with better cognitive performance [52], our study is among the few that considered the ventricular voxels in the analysis.

Other abnormal connectivity changes have also been reported in AD. For instance, previous studies have suggested disrupted functional integration within the cerebellum, DMN, FPN, visual network, and sensorimotor network (SMN) in AD patients compared to controls [59]. Additionally, functional connectivity in the FPN has been found to be significantly reduced in AD compared to controls [50], aligning with our findings. Notably, some studies consider the FPN as a synonym for the Central Executive Network (CEN), while other studies consider the CEN as a part of the FPN but yet a different network. To date, there is no consensus on a unified network taxonomy: some nomenclatures are based on anatomical terminology (*e.g.*, “frontoparietal”, “occipital”), while others refer to network functionality (*e.g.*, “central executive”, “salience”) [56].

In our study, notably, as the number of clusters increases, the “classical” RSNs begin to split into distinct components (e.g., the DMN in K = 17, C = 4, and K = 17, C = 11; see **Figure 4**). Uddin et al. [56] found that, with fine ICA parcellations and an increasing number of clusters, the DMN begins to divide into subsystems: frontal, ventral prefrontal, anterior and medial temporal lobe regions, which further split into additional components as the clustering increases. These findings provide insights into the complexity of the brain's hierarchical organization, which remains an area of speculation. Different methodologies yield varying results, definitions, parcellations, and nomenclatures, contributing to the challenge of consistently replicating the exact results across studies.

All the phase coupling modes we identified included the ventricles, which exhibited a shift from the rest of the brain. We cannot determine whether it is neuronal activity that alters ventricular activity or, conversely, if ventricular pulsations are affecting neuronal activity. Given that the CSF also propagates through the brain parenchyma, our findings do not

exclude the possibility that the ultraslow signals detected in gray matter with fMRI share the same biophysical origin as the signals observed in the ventricles.

Regardless of the direction of influence, the differences we found in the coupling modes are clear and exhibit strong statistical power. Therefore, it is crucial for future research to investigate the origin of this altered signal, as it may contribute to the altered functional connectivity patterns observed in dementia, which may not necessarily originate from neuronal processes.

One important implication of this study is that it challenges the standard preprocessing applied to fMRI data to remove CSF components, and could open up the possibility to re-analyse fMRI datasets. This type of analysis can be applied to virtually all previously recorded 'whole-brain' fMRI scans, but from which the physiological signals have been removed as sources of noise. This allows revisiting old data using a novel analysis framework that could potentially reveal important insights into different neurological disorders and psychiatric syndromes in which the ventricles are altered.

3.2 Limitations

One limitation of this study is the inability to correlate neuroimaging measures with beta-amyloid and tau levels, without sacrificing statistical power due to a lack of available data for all the subjects in the ADNI2 database that we used for the study. The assessments of these measures often preceded the rs-fMRI scans by many years, making direct comparisons unreliable.

Another limitation of the study is given by the relatively poor temporal resolution of the fMRI scans. The TR was 3 seconds, which means that we had a "snapshot" of the brain activities every three seconds. As a result, we cannot rule out the possibility that more rapid fluctuations in brain signals occurred between each snapshot, as suggested by recent research [10,12,14,60,61]. To address this, future studies should consider the use of faster acquisition sequences in fMRI to better detect temporal changes between brain states. A full understanding of these dynamics would require higher temporal resolution, as studies in rats have shown that modes analogous to RSNs are associated with oscillatory stationary waves [14]. This study found that FC modes exhibit an oscillatory dynamic, meaning they switch between positive and negative representations of a pattern—essentially operating in a "push-pull" manner with sustained periodicity, where the timing between positive and negative phases remains constant. This aligns with the emerging wave field theory that

RSNs represent intrinsic resonant modes shaped by brain geometry [62], where these fluctuations appear to contribute to regulating arousal levels [15].

Although our current fMRI methodology lacks the temporal resolution to directly capture these temporal behaviors, the fact that we detected oscillatory brain-ventricle coupling dynamics suggests that ventricles may play a critical role in maintaining these oscillatory mechanisms. Moreover, studies in rodents have already been shown a direct link between neuronal activity and CSF clearance [13]. Our study demonstrates that neurons act as the primary organizers in the process of brain clearance, a discovery that introduces a new theoretical framework for understanding the role of macroscopic brain waves. Moreover, our findings open up new avenues for investigating how ventricles contribute to the broader oscillatory dynamics of the brain, potentially serving as a stabilizing element within these oscillatory patterns.

Another limitation of the study must also consider the impact of brain atrophy that occurs naturally with aging, as many morphological and volumetric changes in the brain are well documented (cfr. [63] for a review). As such, although the MNI template is widely used in studies involving elderly populations, its origin from the brains of young adults may lead to discrepancies in aligning and interpreting brain structures during spatial normalization.

In our sample, the CN are slightly older than the AD patients, which is noteworthy because cognitive decline typically increases with age. If the AD group had been older than the CN group, we could have attributed the differences in RSNs to age-related decline. However, since the AD patients in our study are younger yet still exhibit impaired RSN function, this suggests that the observed network impairments are more likely related to the pathological progression of AD rather than simply to aging.

More importantly, it is now recognized that the clinical and biological presentations of AD do not always coincide. For instance, pathological changes can occur without any clinical manifestation of dementia or MCI [64,65]. For this reason, the International Working Group for New Research Criteria for the Diagnosis of AD, in 2007, proposed new diagnostic criteria, allowing for a diagnosis of AD based on both biological and clinical evidence [66,67]. However, the ADNI 2 inclusion criteria consider only clinical evidence, without accounting for biological markers (for a detailed overview, refer to the ADNI2 procedure manual). Therefore, future studies should use a dataset that includes biological classifications for CN/MCI/AD.

Moreover, the ADNI dataset did not employ specific tools to assess social isolation nor, in general, cognitive reserve. Further analyses utilizing more specific measures such as the

UCLA Loneliness questionnaire or the Cognitive Reserve Index questionnaire (CRIq) could improve the comprehension of the resting state networks associated with these risk factors.

5. Methods

5.1. Study population

The study included 163 unique subjects (32 AD patients, 53 EMCI, 40 LMCI and 38 healthy controls, referred to as “cognitively normal”, CN) from the North American multicenter Alzheimer's Disease Neuroimaging Initiative (ADNI; www.loni.ucla.edu/ADNI). ADNI inclusion and exclusion criteria are detailed at http://www.adni-info.org procedures manual. For our study, we included all the subjects from the ADNI2 phase who had both structural and resting-state functional magnetic resonance imaging (rsfMRI) scans. Demographics of the subjects can be found on **Table 3**.

Each subject had an fMRI scan and behavioral data collected at the baseline visit, and then most of them had follow-up scans and behavioral measurements at 3 months, 6 months, 1 year and 2 years after the baseline visit, resulting in a total of 599 scans.

ADNI (N= 163)	CN (A)	EMCI (B)	LMCI (C)	AD (D)	*p*-values
Sex	17 M, 21 F	21 M, 32 F	24 M, 16 F	15 M, 17 F	A - B = 0.6; A - C = 0.2; A - D = 1; B - C = 0.06; B - D = 0.6; C - D = 0.3
Mean age (SD)	75.5 (7.05)	71.3 (6.55)	72 (8.16)	72.6 (7.2)	**A - B = 0.004**; **A - C = 0.04**; A - D = 0.9; B - C = 0.6; B - D = 0.4; C - D = 0.7
Mean years of education (SD)	16.39 (2.17)	15.6 (2.6)	16.8 (2.43)	15.49 (2.7)	**A - B = 0.002**; A - C = 0.1; **A - D = 0.03**; **B - C = 2e-05**; B - D = 0.7; **C - D = 7e-05**
Marital status	29 MA, 3 DI, 3 W, 3 NM	37 MA, 10 DI, 3 W, 3 NM	30 MA, 1 DI, 8 W, 1 NM	28 MA, 2 DI, 2 W, 0 NM	A - B = 0.5; A - C = 0.2; A - D = 0.4; **B - C = 0.02**; B - D = 0.2; C - D = 0.3
Retirement status	32 R; 6 NR	42 R; 11 NR	34 R; 6 NR	29 R, 3 NR	A - B = 0.6; A - C = 1; A - D = 0.5; B - C = 0.6; B - D = 0.2; C - D = 0.7
Hearing	30 NH, 8 HI	49 NH, 4 HI	36 NH, 4 HI	24 NH, 8 HI	A - B = 0.1; A - C = 0.2; A -

impairment					D = 0.8; B - C = 0.7; **B - D = 0.05**; C - D = 0.1

Table 3. Baseline characteristics of 163 unique subjects from ADNI used in this study. p-values are derived from 2-sample t-tests for continuous measures, and Fisher's exact test for categorical measures. Statistically significant differences ($p < 0.05$) in each comparison were marked using a bold format.
AD = Alzheimer disease participants; ADNI = Alzheimer's Disease Neuroimaging Initiative; CN = cognitively normal; DI = divorced; EMCI, early mild cognitive impairment; HI = hearing impairment; LMCI = late mild cognitive impairment; M/F = male/female; MA = married; NH = normal hearing; NM = non married; NR = not retired from work; R = retired from work; SD = standard deviation; W = widowed

5.2. Years of education and social isolation

The progression into dementia is related to specific risk factors, amounting to 12 according to the latest work by the Lancet Commission: lower education, hearing loss, traumatic brain injury, hypertension, alcohol abuse, obesity, smoking, depression, social isolation, physical inactivity, diabetes and air pollution [54]. Among these factors, lower education is the one that most relates to the onset of dementia, with a relative risk of 1.6% and a prevalence of 40% [54]. On the other hand, social isolation, while alone seems to account for 1.6% of relative risk and 28.1% prevalence, in older adults seems to be correlated with diminished quality of life, reduced life satisfaction, and heightened susceptibility to depression [68], which accounts for 1.9% of relative risk. Moreover, social isolation is also amplified by hearing impairment [69], which accounts for 1.9% of relative risk factors with a prevalence of 31.7%, up to approximately 60% in individuals aged 65 and above [70].

We extracted the years of education from the ADNI database for determining how this risk factor would impact functional connectivity metrics. This variable is often used as a proxy for cognitive reserve in the literature [71].

Since the ADNI database does not include specific tests to measure social isolation, we score to marital status, retirement status, presence of hearing impairment,. Specifically, information on marital and employment status was extracted from the ADNI Subject Demographics table (specifically, the PTMARRY and PTNOTRT columns). The values for hearing impairment were obtained by comparing reports in the Neurological Exam, Physical Exam, and Recent Medical History Details Log tables, as done by Llano et al. [72].

Retirement status (PTWORK) was assessed, assigning a score of 1 to retired individuals and 0 to those who are still employed. Second, marital status (PTMARRY) was considered, with a score of 1 given to individuals who are unmarried, divorced, or widowed, and a score of 0 to those who are married. Finally, hearing ability was included in the scale, where a score of 1 represents hearing loss and 0 represents normal hearing ability.

1. Is the subject unmarried/divorced/widowed? Yes (1), No (0)
2. Is the subject retired from work? Yes (1), No (0)
3. Does the subject experience hearing loss? Yes (1), No (0)

5.3. Phenotypic Harmonization Consortium cognitive scores

To examine relations between mode occupancy and cognitive performance, we used the ADNI cognitive composite scores, which integrate multiple neuropsychological tests including the Mini Mental State Examination (MMSE), Montreal Cognitive Assessment (MoCA), and Alzheimer's Disease Assessment Scale – Cognitive Subscale (ADAS-Cog) into four cognitive domains:

- *Memory (ADNI-Mem)*: This composite score incorporates the Rey Auditory Verbal Learning Test (RAVLT), ADAS-Cog Word Recall, Delayed Word Recall, Orientation, and Word Recognition, Logical Memory (immediate and delayed) from the Wechsler Memory Scale-Revised (WMS-R), relevant MMSE items (immediate recall, delayed recall, orientation), and MoCA delayed recall and registration scores [73].
- *Executive Function (ADNI-EF)*: This composite includes the Clock Drawing Test (CDT) command scores, Trail Making Test (TMT), Wechsler Adult Intelligence Scale-Revised (WAIS-R) Digit Span (Forward and Backward) and Digit Symbol tasks, ADAS-Cog number cancellation, MMSE backward spelling, and relevant MoCA executive function items [74].
- *Visuospatial Function (ADNI-VS)*: This composite incorporates CDT copy tasks, ADAS-Cog Constructional Praxis, and MMSE drawing tasks [74].
- *Language (ADNI-Lan)*: This composite includes Category Fluency (Animals/Vegetables), Boston Naming Test (BNT), and language-related items from the MoCA, MMSE, and ADAS-Cog [74].

These composites were psychometrically optimized to maximize measurement precision while minimizing floor and ceiling effects. Higher scores indicate better cognitive performance across all domains. These 4 composite scores were obtained at most but not all fMRI sessions, resulting in 447 fMRI scans with associated Memory score, 443 scans with Executive Function score, 465 scans with Language score and 273 scans with Visuospatial score.

5.4. MRI acquisition parameters

All MRI data from the ADNI study were acquired using 3 Tesla MR scanners at various participating sites, following the standardized ADNI2 protocol. The scanners used were from recent models produced by General Electric (GE, Chicago, United States), Philips Medical Systems (Philips, Amsterdam, Netherlands), and Siemens Medical Solutions (Siemens, Erlangen, Germany) (full acquisition details can be found at http://adni.loni.usc.edu/methods/documents/mri-protocols/).

rsfMRI volumes were collected with an echo-planar image (EPI) sequence (flip angle = 80°, spatial resolution = 3 × 3 × 3 mm3, slice thickness = 3.3 mm; with TR/TE (repetition time / echo time) = 3000/30 ms. Each fMRI scan lasted 7 minutes. In addition we used an MPRAGE sequence TR/TE = 2300/3.1 ms, which was used for anatomical segmentation and template normalization.

5.5. fMRI preprocessing

The fMRI data preprocessing was conducted using CONN's default pipeline for volume-based analyses with direct normalization to MNI-space [75]. This pipeline encompasses five main steps:

1. Functional realignment and unwarping: Using SPM12's realign & unwarp procedure [76], all volumes were coregistered to the first (reference) volume using b-spline interpolation. This step also compensates for susceptibility distortion-by-motion interactions by computing deformation field derivatives relative to head movement.
2. Slice-timing correction: The functional data underwent temporal alignment using SPM12 with sinc-interpolation.
3. Quality control: The pipeline identified outliers by detecting global fMRI signal changes exceeding 5 standard deviations and framewise displacement greater than 0.9mm.
4. Spatial normalization: Both functional (rsfMRI) and structural (T1-weighted MPRAGE) images were normalized to MNI space using SPM12's unified segmentation and normalization algorithm [77]. This direct normalization process used a 180x216x180mm bounding box, with 2mm and 1mm isotropic voxels for functional and anatomical data respectively, implemented with 4th order spline interpolation.
5. Spatial smoothing: The final step applied an 8mm FWHM Gaussian kernel to the functional data to minimize inter-subject variability in functional and gyral anatomy.

The first 5 volumes in each rsfMRI scan were discarded to eliminate nonsteady-state effects that occur while the signal reaches equilibrium at the start of each functional run. The voxel time-series were then bandpass filtered between 0.01-0.1 Hz to isolate the low-frequency fluctuations which have been shown to correlate over long distances, while removing components from cardiac and respiratory cycles (>0.1 Hz) and scanner drift (<0.01 Hz) [78,79].

5.6. fMRI data analysis

Given the particular goal of this study to analyze fMRI signals from the brain, irrespective of their anatomical location, instead of averaging the fMRI signals into Regions-of-Interest (ROI) defined from a parcellation template, we opted instead to perform the analysis considering each cubic voxel inside the MNI brain mask of as a ROI. We considered the MNI template with 1 cubic centimeter voxels, which contains N=1821 voxels covering the entire brain. The fMRI volumes from each subject - already aligned in MNI space - were then downsampled from $2mm^3$ to $10mm^3$ using linear interpolation, and the N=1821 voxels inside the MNI brain mask were treated as brain parcels. This downsampling is acceptable given that i) the signals were spatially smoothed with a gaussian kernel of 8mm in preprocessing steps and ii) the high variability between subjects is reduced with larger voxels.

To investigate the existence of recurrent phase-coupling modes, and whether their occurrence varied with AD progression, we applied the Leading Eigenvector Dynamics Analysis (LEiDA) methodology [52]. Following the LEiDA algorithm, the Hilbert transform was applied to the 1xT time series in each of the N=1821 voxel time series to extract the fMRI signal phase θ in each voxel. For each time instant (between t=2 and t=T-1), we compute the 1xN leading eigenvector of the N × N matrix of phase coherence (obtained using $\cos(\theta(n, t) - \theta(p, t)$, with n and p corresponding to all the N=1821 voxels). A total of 81707 'instantaneous' leading eigenvectors was obtained from all the 599 scans, each representing how the fMRI signals in all the N voxels are organized in terms of phase relationship at each instant of time.

These leading eigenvectors, which represent snapshots of phase relationships observed across scans at all time points, were then categorized into K clusters through k-means clustering, using the cosine distance to evaluate the cluster-to-centroid distance. Given the unpredictability of the precise number of functional coupling modes, K was varied from 2 to 20, and the results were analyzed across the explored partition range, ensuring result stability with 500 replicates of k-means [52,80].

The clustering assigns a single cluster/mode to each time point by selecting the closest centroid at each time point. Using these cluster time courses, we calculated the Occupancy of each mode in each scan, which is the number of time points assigned to a given state divided by the total number of time points (TRs) in each scan. The occupancies of each mode were calculated for each scan across different partition models, with k ranging from 2 to 20 [52].

5.7. Statistical analyses

To detect functional states whose probability of occurrence differs significantly among groups, we used a permutation-based paired *t*-test. This non-parametric test uses permutations of group labels to estimate the null distribution, which is computed independently for each experimental condition. A t-test is conducted for each of the 10,000 permutations to compare populations, resulting in a p-value for each comparison.

We evaluated the statistical significance of our results considering the FWER by plotting the p-values against various significance thresholds. Specifically, we used the standard threshold of $\alpha 1 = 0.05$ (shown in red), the Bonferroni corrected threshold $\alpha 2 = 0.05/k$ (shown in green) to correct for the number of independent hypotheses tested in each partition model (with $\alpha 2$ decreasing as k increases), and $\alpha 3 = 0.05/\sum(k=2:k=25)=0{,}00015$, which conservatively adjusts for all comparisons, whether dependent or independent.

Given that multiple modes were compared, which increases the chances of false positives, we consider only the modes whose difference between groups survives correction for multiple comparisons.

To detect functional states whose probability of occurrence correlates with the different scores of years of education and social isolation, we computed Pearson's correlation between the probability of occurrence in every scan with the corresponding score.

5.8 Visualization of cluster centroids

The cluster centroids are 1xN vectors, where each of the N=1821 elements corresponds to a cubic centimeter voxel in the brain. The cluster centroids obtained in $10mm^3$ were resized to $2mm^3$ using a linear interpolation for better visualization. Using concepts from analytic geometry, the values in each vector element refer to the projection (*i.e.*, cosine of the phase) of each voxel into the leading eigenvector, which defines the main orientation of all signal phases. The sign of the vector elements depends on whether the phase difference (to the leading eigenvector) is smaller or larger than 90°. As such, grouping all the voxels according

to their sign in the cluster centroid, reveals two communities, where the smallest community reveals the brain areas varying in anti-phase with the rest of the brain.

5.9 Overlap with RSNs

The overlap with seven reference intrinsic connectivity networks (ICNs) [55] was then calculated for each of the cluster centroids obtained. Given that the template of 7 ICNs is available in $2mm^3$ MNI space, the cluster centroids obtained in $10mm^3$ were resized to $2mm^3$ and the overlap was calculated by computing the Pearson correlation between the binary masks of each network (considering only cortical voxels) with the corresponding binary mask of the cluster centroids (setting 1 to all the voxels with positive value in the leading eigenvector and 0 otherwise). The cluster centroids were colored with the original paper's color scheme [55].

Acknowledgements

Data collection and sharing for this project was funded by the Alzheimer's Disease Neuroimaging Initiative (ADNI) (National Institutes of Health Grant U01 AG024904) and DoD ADNI (Department of Defense award number W81XWH-12-2-0012). ADNI is funded by the National Institute on Aging, the National Institute of Biomedical Imaging and Bioengineering, and through generous contributions from the following: AbbVie, Alzheimer's Association; Alzheimer's Drug Discovery Foundation; Araclon Biotech; BioClinica, Inc.; Biogen; Bristol-Myers Squibb Company; CereSpir, Inc.; Cogstate; Eisai Inc.; Elan Pharmaceuticals, Inc.; Eli Lilly and Company; EuroImmun; F. Hoffmann-La Roche Ltd and its affiliated company Genentech, Inc.; Fujirebio; GE Healthcare; IXICO Ltd.; Janssen Alzheimer Immunotherapy Research & Development, LLC.; Johnson & Johnson Pharmaceutical Research & Development LLC.; Lumosity; Lundbeck; Merck & Co., Inc.; Meso Scale Diagnostics, LLC.; NeuroRx Research; Neurotrack Technologies; Novartis Pharmaceuticals Corporation; Pfizer Inc.; Piramal Imaging; Servier; Takeda Pharmaceutical Company; and Transition Therapeutics. The Canadian Institutes of Health Research is providing funds to support ADNI clinical sites in Canada. Private sector contributions are facilitated by the Foundation for the National Institutes of Health (www.fnih.org). The grantee organization is the Northern California Institute for Research and Education, and the study is coordinated by the Alzheimer's Therapeutic Research Institute at the University of Southern California. ADNI data are disseminated by the Laboratory for Neuro Imaging at the University of Southern California.

The Center for Music in the Brain (MIB) is funded by the Danish National Research Foundation (project number DNRF117).

FFC Ph.D. Scholarship was funded by POR Puglia FESR FSE 2014-2020, CUP: H99121006630008.

SN is supported by the Italian Ministry of Research, under the complementary actions to the NRRP "Fit4MedRob - Fit for Medical Robotics" Grant (# PNC0000007).

This publication was also produced with the co-funding European Union - Next Generation EU, in the context of The National Recovery and Resilience Plan, Investment Partenariato Esteso PE8 "Conseguenze e sfide dell'invecchiamento", Project Age-It (Ageing Well in an Ageing Society), CUP: B83C22004800006.

JC is supported by La Caixa Foundation, Spain (LCF/BQ/PR22/11920014) and the Foundation for Science and Technology, Portugal (UIDB/50026/2020, UIDP/50026/2020).

CRediT Author Statement

FFC: Investigation, Formal analyses, Data curation, Writing - Original Draft, Writing - Review & Editing; **EB:** Conceptualization, Supervision, Writing - Review & Editing; **VM:** Formal analyses, Writing - Review & Editing (contribution to section 5.3); **SN:** Writing - Review & Editing; **BT:** Writing - Review & Editing; **GL:** Supervision, Writing - Review & Editing; **JC:** Conceptualization, Supervision, Methodology, Software, Formal analyses, Data Curation, Visualization, Writing - Original Draft, Writing - Review & Editing.

References

1. Blennow, K. & Zetterberg, H. Biomarkers for Alzheimer's disease: current status and prospects for the future. *J. Intern. Med.* **284**, 643–663 (2018).
2. Sperling, R. A. *et al.* Toward defining the preclinical stages of Alzheimer's disease: recommendations from the National Institute on Aging-Alzheimer's Association workgroups on diagnostic guidelines for Alzheimer's disease. *Alzheimers. Dement.* **7**, 280–292 (2011).
3. Jack, C. R., Jr *et al.* NIA-AA Research Framework: Toward a biological definition of Alzheimer's disease. *Alzheimers. Dement.* **14**, 535–562 (2018).
4. Cirrito, J. R. *et al.* Synaptic activity regulates interstitial fluid amyloid-beta levels in vivo. *Neuron* **48**, 913–922 (2005).
5. Yamada, K. *et al.* In vivo microdialysis reveals age-dependent decrease of brain interstitial fluid tau levels in P301S human tau transgenic mice. *J. Neurosci.* **31**, 13110–13117 (2011).
6. Iliff, J. J. *et al.* A paravascular pathway facilitates CSF flow through the brain parenchyma and the clearance of interstitial solutes, including amyloid β. *Sci. Transl. Med.* **4**, 147ra111 (2012).
7. Iliff, J. J. *et al.* Brain-wide pathway for waste clearance captured by contrast-enhanced MRI. *J. Clin. Invest.* **123**, 1299–1309 (2013).
8. Xie, L. *et al.* Sleep drives metabolite clearance from the adult brain. *Science* **342**, 373–377 (2013).
9. Han, F., Liu, X., Mailman, R. B., Huang, X. & Liu, X. Resting-state global brain activity affects early β-amyloid accumulation in default mode network. *Nat. Commun.* **14**, 7788 (2023).
10. Fultz, N. E. *et al.* Coupled electrophysiological, hemodynamic, and cerebrospinal fluid oscillations in human sleep. *Science* **366**, 628–631 (2019).
11. Han, F. *et al.* Reduced coupling between cerebrospinal fluid flow and global brain

activity is linked to Alzheimer disease-related pathology. *PLoS Biol.* **19**, e3001233 (2021).

12. Kiviniemi, V. *et al.* Ultra-fast magnetic resonance encephalography of physiological brain activity - Glymphatic pulsation mechanisms? *J. Cereb. Blood Flow Metab.* **36**, 1033–1045 (2016).
13. Jiang-Xie, L.-F. *et al.* Neuronal dynamics direct cerebrospinal fluid perfusion and brain clearance. *Nature* **627**, 157–164 (2024).
14. Cabral, J., Fernandes, F. F. & Shemesh, N. Intrinsic macroscale oscillatory modes driving long range functional connectivity in female rat brains detected by ultrafast fMRI. *Nat. Commun.* **14**, 375 (2023).
15. Raut, R. V. *et al.* Global waves synchronize the brain's functional systems with fluctuating arousal. *Sci. Adv.* **7**, eabf2709 (2021).
16. Chen, J. E. *et al.* Resting-state 'physiological networks'. *Neuroimage* **213**, 116707 (2020).
17. Cabral, J., Kringelbach, M. L., & Deco, G. Functional connectivity dynamically evolves on multiple time-scales over a static structural connectome: Models and mechanisms. *Neuroimage* **160**, 84–96 (2017).
18. Atasoy, S., Donnelly, I. & Pearson, J. Human brain networks function in connectome-specific harmonic waves. *Nat. Commun.* **7**, 10340 (2016).
19. Pang, W. *et al.* Visual deprivation alters functional connectivity of neural networks for voice recognition: A resting-state fMRI study. *Brain Sci.* **13**, 636 (2023).
20. Liu, X., Zhang, N., Chang, C. & Duyn, J. H. Co-activation patterns in resting-state fMRI signals. *Neuroimage* **180**, 485–494 (2018).
21. Lv, H. *et al.* Resting-State Functional MRI: Everything That Nonexperts Have Always Wanted to Know. *AJNR Am. J. Neuroradiol.* **39**, 1390–1399 (2018).
22. Fox, M. D. *et al.* The human brain is intrinsically organized into dynamic, anticorrelated functional networks. *Proc. Natl. Acad. Sci. U. S. A.* **102**, 9673–9678 (2005).
23. Grieder, M., Wang, D. J. J., Dierks, T., Wahlund, L.-O. & Jann, K. Default Mode Network

Complexity and Cognitive Decline in Mild Alzheimer's Disease. *Front. Neurosci.* **12**, 770 (2018).

24. Cha, J. *et al.* Functional alteration patterns of default mode networks: comparisons of normal aging, amnestic mild cognitive impairment and Alzheimer's disease. *Eur. J. Neurosci.* **37**, 1916–1924 (2013).
25. Ouchi, Y. & Kikuchi, M. A review of the default mode network in aging and dementia based on molecular imaging. *Rev. Neurosci.* **23**, 263–268 (2012).
26. Ibrahim, B. *et al.* Diagnostic power of resting-state fMRI for detection of network connectivity in Alzheimer's disease and mild cognitive impairment: A systematic review. *Hum. Brain Mapp.* **42**, 2941–2968 (2021).
27. Brier, M. R. *et al.* Loss of intranetwork and internetwork resting state functional connections with Alzheimer's disease progression. *J. Neurosci.* **32**, 8890–8899 (2012).
28. Gili, T. *et al.* Regional brain atrophy and functional disconnection across Alzheimer's disease evolution. *J. Neurol. Neurosurg. Psychiatry* **82**, 58–66 (2011).
29. Griffanti, L. *et al.* Effective artifact removal in resting state fMRI data improves detection of DMN functional connectivity alteration in Alzheimer's disease. *Front. Hum. Neurosci.* **9**, 449 (2015).
30. Seoane, S., van den Heuvel, M., Acebes, Á. & Janssen, N. The subcortical default mode network and Alzheimer's disease: a systematic review and meta-analysis. *Brain Commun* **6**, fcae128 (2024).
31. Aguilar, D. D. & McNally, J. M. Subcortical control of the default mode network: Role of the basal forebrain and implications for neuropsychiatric disorders. *Brain Res. Bull.* **185**, 129–139 (2022).
32. Harrison, B. J. *et al.* Dynamic subcortical modulators of human default mode network function. *Cereb. Cortex* **32**, 4345–4355 (2022).
33. Munn, B. R., Müller, E. J., Wainstein, G. & Shine, J. M. The ascending arousal system shapes neural dynamics to mediate awareness of cognitive states. *Nat. Commun.* **12**, 6016 (2021).

34. Xue, J. *et al.* Altered Directed Functional Connectivity of the Hippocampus in Mild Cognitive Impairment and Alzheimer's Disease: A Resting-State fMRI Study. *Front. Aging Neurosci.* **11**, 326 (2019).
35. Allen, G. *et al.* Reduced hippocampal functional connectivity in Alzheimer disease. *Arch. Neurol.* **64**, 1482–1487 (2007).
36. Westlye, E. T., Lundervold, A., Rootwelt, H., Lundervold, A. J. & Westlye, L. T. Increased hippocampal default mode synchronization during rest in middle-aged and elderly APOE ε4 carriers: relationships with memory performance. *J. Neurosci.* **31**, 7775–7783 (2011).
37. Tang, F. *et al.* Differences Changes in Cerebellar Functional Connectivity Between Mild Cognitive Impairment and Alzheimer's Disease: A Seed-Based Approach. *Front. Neurol.* **12**, 645171 (2021).
38. Yao, H. *et al.* Decreased functional connectivity of the amygdala in Alzheimer's disease revealed by resting-state fMRI. *Eur. J. Radiol.* **82**, 1531–1538 (2013).
39. Zhou, B. *et al.* Impaired functional connectivity of the thalamus in Alzheimer's disease and mild cognitive impairment: a resting-state fMRI study. *Curr. Alzheimer Res.* **10**, 754–766 (2013).
40. Blessing, E. M., Beissner, F., Schumann, A., Brünner, F. & Bär, K.-J. A data-driven approach to mapping cortical and subcortical intrinsic functional connectivity along the longitudinal hippocampal axis. *Hum. Brain Mapp.* **37**, 462–476 (2016).
41. Buckner, R. L., Krienen, F. M., Castellanos, A., Diaz, J. C. & Yeo, B. T. T. The organization of the human cerebellum estimated by intrinsic functional connectivity. *J. Neurophysiol.* **106**, 2322–2345 (2011).
42. Kawabata, K. *et al.* Functional connector hubs in the cerebellum. *Neuroimage* **257**, 119263 (2022).
43. Bernard, J. A. *et al.* Dissociable functional networks of the human dentate nucleus. *Cereb. Cortex* **24**, 2151–2159 (2014).
44. Alves, P. N. *et al.* An improved neuroanatomical model of the default-mode network reconciles previous neuroimaging and neuropathological findings. *Commun Biol* **2**, 370

(2019).

45. Li, J. *et al.* Mapping the subcortical connectivity of the human default mode network. *Neuroimage* **245**, 118758 (2021).
46. Wang, Z. *et al.* Differentially disrupted functional connectivity of the subregions of the amygdala in Alzheimer's disease. *J. Xray Sci. Technol.* **24**, 329–342 (2016).
47. Sridharan, D., Levitin, D. J. & Menon, V. A critical role for the right fronto-insular cortex in switching between central-executive and default-mode networks. *Proc. Natl. Acad. Sci. U. S. A.* **105**, 12569–12574 (2008).
48. He, X. *et al.* Abnormal salience network in normal aging and in amnestic mild cognitive impairment and Alzheimer's disease. *Hum. Brain Mapp.* **35**, 3446–3464 (2014).
49. Agosta, F. *et al.* Resting state fMRI in Alzheimer's disease: beyond the default mode network. *Neurobiol. Aging* **33**, 1564–1578 (2012).
50. Zhao, Q., Lu, H., Metmer, H., Li, W. X. Y. & Lu, J. Evaluating functional connectivity of executive control network and frontoparietal network in Alzheimer's disease. *Brain Res.* **1678**, 262–272 (2018).
51. Zhao, Q. *et al.* Functional segregation of executive control network and frontoparietal network in Alzheimer's disease. *Cortex* **120**, 36–48 (2019).
52. Cabral, J. *et al.* Cognitive performance in healthy older adults relates to spontaneous switching between states of functional connectivity during rest. *Sci. Rep.* **7**, 1–13 (2017).
53. Beckett, L. A. *et al.* The Alzheimer's Disease Neuroimaging Initiative phase 2: Increasing the length, breadth, and depth of our understanding. *Alzheimers. Dement.* **11**, 823–831 (2015).
54. Livingston, G. *et al.* Dementia prevention, intervention, and care: 2020 report of the Lancet Commission. *Lancet* **396**, 413–446 (2020).
55. Yeo, B. T. T. *et al.* The organization of the human cerebral cortex estimated by intrinsic functional connectivity. *J. Neurophysiol.* **106**, 1125–1165 (2011).
56. Uddin, L. Q. *et al.* Controversies and progress on standardization of large-scale brain network nomenclature. *Netw. Neurosci.* **7**, 864–905 (2023).

57. McKenna, F., Koo, B.-B., Killiany, R. & Alzheimer's Disease Neuroimaging Initiative. Comparison of ApoE-related brain connectivity differences in early MCI and normal aging populations: an fMRI study. *Brain Imaging Behav.* **10**, 970–983 (2016).
58. Ahmadi, H., Fatemizadeh, E. & Motie-Nasrabadi, A. Identifying brain functional connectivity alterations during different stages of Alzheimer's disease. *Int. J. Neurosci.* **132**, 1005–1013 (2022).
59. Zheng, W., Liu, X., Song, H., Li, K. & Wang, Z. Altered Functional Connectivity of Cognitive-Related Cerebellar Subregions in Alzheimer's Disease. *Front. Aging Neurosci.* **9**, 143 (2017).
60. Dowdle, L. T. *et al.* Statistical power or more precise insights into neuro-temporal dynamics? Assessing the benefits of rapid temporal sampling in fMRI. *Prog. Neurobiol.* **207**, 102171 (2021).
61. Palmer, W. C., Park, S. M. & Levendovszky, S. R. Brain state transition analysis using ultra-fast fMRI differentiates MCI from cognitively normal controls. *Front. Neurosci.* **16**, 975305 (2022).
62. Pang, J. C. *et al.* Geometric constraints on human brain function. *Nature* **618**, 566–574 (2023).
63. MacDonald, M. E. & Pike, G. B. MRI of healthy brain aging: A review. *NMR Biomed.* **34**, e4564 (2021).
64. Bennett, D. A. *et al.* Neuropathology of older persons without cognitive impairment from two community-based studies. *Neurology* **66**, 1837–1844 (2006).
65. Knopman, D. S. *et al.* Neuropathology of cognitively normal elderly. *J. Neuropathol. Exp. Neurol.* **62**, 1087–1095 (2003).
66. Dubois, B. *et al.* Revising the definition of Alzheimer's disease: a new lexicon. *Lancet Neurol.* **9**, 1118–1127 (2010).
67. Dubois, B. *et al.* Research criteria for the diagnosis of Alzheimer's disease: revising the NINCDS-ADRDA criteria. *Lancet Neurol.* **6**, 734–746 (2007).
68. Gerino, E., Rollè, L., Sechi, C. & Brustia, P. Loneliness, Resilience, Mental Health, and

Quality of Life in Old Age: A Structural Equation Model. *Front. Psychol.* **8**, 2003 (2017).

69. Shukla, A. *et al.* Hearing Loss, Loneliness, and Social Isolation: A Systematic Review. *Otolaryngol. Head Neck Surg.* **162**, 622–633 (2020).
70. Dror, A. A. & Avraham, K. B. Hearing impairment: a panoply of genes and functions. *Neuron* **68**, 293–308 (2010).
71. Staekenborg, S. S. *et al.* Education as Proxy for Cognitive Reserve in a Large Elderly Memory Clinic: 'Window of Benefit'. *J. Alzheimers. Dis.* **76**, 671–679 (2020).
72. Llano, D. A., Kwok, S. S., Devanarayan, V. & The Alzheimer's Disease Neuroimaging Initiative (ADNI). Reported Hearing Loss in Alzheimer's Disease Is Associated With Loss of Brainstem and Cerebellar Volume. *Front. Hum. Neurosci.* **15**, 739754 (2021).
73. Crane, P. K. *et al.* Development and assessment of a composite score for memory in the Alzheimer's Disease Neuroimaging Initiative (ADNI). *Brain Imaging Behav* **6**, 502–516 (2012).
74. Gibbons, L. E. *et al.* A composite score for executive functioning, validated in Alzheimer's Disease Neuroimaging Initiative (ADNI) participants with baseline mild cognitive impairment. *Brain Imaging Behav* **6**, 517–527 (2012).
75. Nieto-Castanon, A. *Handbook of Functional Connectivity Magnetic Resonance Imaging Methods in CONN*. (Hilbert Press, 2020).
76. Andersson, J. L. R., Hutton, C., Ashburner, J., Turner, R. & Friston, K. Modeling Geometric Deformations in EPI Time Series. *NeuroImage* **13**, 903–919 (2001).
77. Ashburner, J. & Friston, K. J. Unified segmentation. *Neuroimage* **26**, 839–851 (2005).
78. Biswal, B., Yetkin, F. Z., Haughton, V. M. & Hyde, J. S. Functional connectivity in the motor cortex of resting human brain using echo-planar MRI. *Magn. Reson. Med.* **34**, 537–541 (1995).
79. Cordes, D. *et al.* Frequencies contributing to functional connectivity in the cerebral cortex in 'resting-state' data. *AJNR Am J Neuroradiol* **22**, 1326–1333 (2001).
80. Vohryzek, J., Deco, G., Cessac, B., Kringelbach, M. L. & Cabral, J. Ghost Attractors in Spontaneous Brain Activity: Recurrent Excursions Into Functionally-Relevant BOLD

Phase-Locking States. *Front. Syst. Neurosci.* **14**, 518364 (2020).